Computational Particle Mechanics (2021) 8:215–235
https://doi.org/10.1007/s40571-020-00325-6

Realistic soil particle generation based on limited morphological information by probability-based spherical harmonics

Quan Sun[1] · Junxing Zheng[1]

Received: 25 October 2019 / Revised: 1 February 2020 / Accepted: 28 February 2020 / Published online: 10 March 2020

Abstract
Three-dimensional imaging techniques, such as X-ray computed tomography, have been used to scan realistic particle geometries. However, these techniques are labor intensive, time-consuming, and costly to obtain a large number of particles. Therefore, it is desirable if computers can be taught to generate realistic particles based on given morphological properties. This paper develops a particle generation technique by integrating spherical harmonics and probability functions. This technique only requires morphological information from one particle to generate a large number of particles and eliminates the need for scanning many particles for particle generation. The spherical harmonics coefficients of this particle are analog of the morphological gene. The probability function is used to add variances to spherical harmonics coefficients to simulate gene mutation. A dimensionless factor is developed to control degrees of gene mutation. The effectiveness and accuracy of the proposed technique are verified by particle shape descriptors computed by the computational geometry techniques.

Keywords Realistic particle generation · Spherical harmonics · Probability function · Morphological properties

1 Introduction

Particle shape profoundly affects the engineering behavior of coarse-grained soils. Experimental studies have shown that angular and elongated particles exhibit larger values of index void ratios, internal friction, dilatancy, constant volume friction angle, compressibility, and small-strain modulus than rounded and spherical soils [1–14]. With the development of computer modeling in geotechnical engineering, the discrete element method (DEM) has become a popular method to investigate the relationship between micro-level particle morphology and macro-mechanical behavior of granular soils. However, the typical DEM uses spherical approximations rather than the actual particle shapes to simulate individual particles, which cannot provide adequately accurate insight into the mechanical behavior of granular soils consisting of non-spherical particles [15, 16].

Three-dimensional (3D) imaging techniques have considerably advanced in the last two decades, which have been used by geotechnical engineers to scan three-dimensional (3D) realistic particle geometries for DEM simulations and other analytical research. Therefore, many 3D imaging techniques have been used in geotechnical engineering, such as X-ray computed tomography (X-ray CT) [17–23], laser scanning technique [24–26], optical interferometer [27, 28], stereophotography [29–31], and structured light technique [32].

X-ray computed tomography (CT) is an ideal technique to scan 3D particle geometries. However, the sizes of soil specimens for X-ray CT scans are typically approximately 12 mm in diameter and 24 mm in height [17–22]. Therefore, scanning a sufficient amount of soil particles for performing a triaxial test simulation (diameter = 50 mm, height = 100 mm) requires approximately 70 scans. In addition, analyzing X-ray CT images to separate air and solid particles requires extensive image processing skills and demanding computational efforts. Therefore, it is not efficient to perform many X-ray CT scans. A more feasible

✉ Junxing Zheng
junxing@iastate.edu

Quan Sun
quansun@iastate.edu

[1] Department of Civil, Construction and Environmental Engineering, Iowa State University, Ames, IA 50011, USA

approach to generate realistic particles is to do one, or several of X-ray CT scans to obtain shape characterizations, and then use these characteristics to generate as many particles as necessary for DEM simulations [33].

Many algorithms have been developed to generate realistic particles. Most of these algorithms were based on spherical harmonics techniques. For example, Grigoriu et al. [34] made early attempts to use spherical harmonics techniques to generate realistic aggregates for concrete. Liu et al. [23] combined spherical harmonics with random field theory for sand particle generations. Zhou et al. [35] combined spherical harmonics and principal component analysis to generate realistic particles. Wei et al. [36] combined spherical harmonics with fractal dimension to generate realistic particles. Su and Yan [37] combined spherical harmonic with multivariate random vector techniques to generate realistic particles. These excellent works enabled computers to generate realistic particles for DEM simulations and other mechanical analysis.

These existing studies aimed to generate random particles but with similar morphology to a target soil particle. The spherical harmonics technique was used to analyze a large number of particles from a granular soil to extract morphological properties. Then, the morphological property was used to generate as many particles as necessary. This research aimed to clone a single particle. This was challenging because only limited morphological property from a single particle was available. This research addressed this issue by developing a novel probability-based spherical harmonics technique. The spherical harmonics coefficients were extracted from the particle geometry to identify the morphological property, which is analog of the "morphological gene" of this particle. Then, the probability function was used to add variances to spherical harmonics coefficients to create "gene mutation" to morphological gene, which enabled a computer to generate random morphological variances in the generated particles to create different particle shapes. A dimensionless factor was defined to control the degree of gene mutation. Users can tune the controlling factor to determine the morphological variation of generated particles against the original particle.

The proposed probability-based spherical harmonics technique was simple, effective, and versatile. This technique generated particle based on the morphological property of single particle and eliminated the need for scanning many particles for particle generation.

This paper starts with an introduction to two-dimensional (2D) curve representation by the Fourier series as a simple version of the 3D surface representation by spherical harmonics. Then, this paper integrates spherical harmonics and probability function to develop the probability-based spherical harmonics techniques for generating realistic particles. A series of computational geometry techniques are introduced in this paper to determine particle shape descriptors as a measure of morphological variances. Finally, the effectiveness and accuracy of the proposed technique are validated by comparing particle shapes between generated particles and original particles.

2 Fourier series for representing a 2D curve

Fourier series can be used to represent the 2D curves [38, 39]. Therefore, the perimeter of a 2D particle can be represented by Fourier series $f(t)$, using sines and cosines functions:

$$f_n(t) = \frac{a_0}{2} + \sum_{n=1}^{N} \left(a_n \cos\left(\frac{2\pi t}{T}\right) + b_n \sin\left(\frac{2\pi t}{T}\right) \right) \tag{1}$$

where T is the period of the function; t is time; and a_n, b_n are the Fourier coefficients,

$$\begin{cases} a_n = \dfrac{2}{T} \displaystyle\int_T f(t) \cos\left(2\pi t \frac{n}{T}\right) \mathrm{d}x \\ b_n = \dfrac{2}{T} \displaystyle\int_T f(t) \sin\left(2\pi t \frac{n}{T}\right) \mathrm{d}x. \end{cases} \tag{2}$$

For example, Fig. 1 illustrates different representations of a rectangle by Fourier series:

$$f_n(t) = \frac{4}{\pi} \left[\cos(\omega_0 t) - \frac{1}{3}\cos(3\omega_0 t) + \frac{1}{5}\cos(5\omega_0 t) + \cdots + (-1)^{\frac{n-1}{2}} \cos(n \cdot \omega_0 t) + \cdots \right] \tag{3}$$

where $\omega_0 = 2\pi/T$ is the angular velocity and n is frequency. No sines bases in this function since the rectangle is axial symmetry by y axis (amplitude direction). Therefore, terms with even n values equal zero. As the n increasing, the higher frequency terms are included in $f(t)$ function, so the reconstructed rectangle by $f(t)$ is closer to the original rectangle as shown in Fig. 1.

Figure 2 shows the Fourier expansion of Eq. (3) in the time domain, frequency domain, and phase spectrum. Each term in Eq. 3 represents a cosine curve at different frequency n values and different amplitudes as shown in Fig. 2. The superposition of all the cosine curves on the time domain represents the original rectangle shape. The shape in the time domain can be projected onto frequency domain, which defines the relationship between frequency n and amplitude. The time domain image can also be projected onto the phase plane. Each red dot on the phase spectrum indicates the position of first wave crest at different n values. In this example, lengths of bars at even n

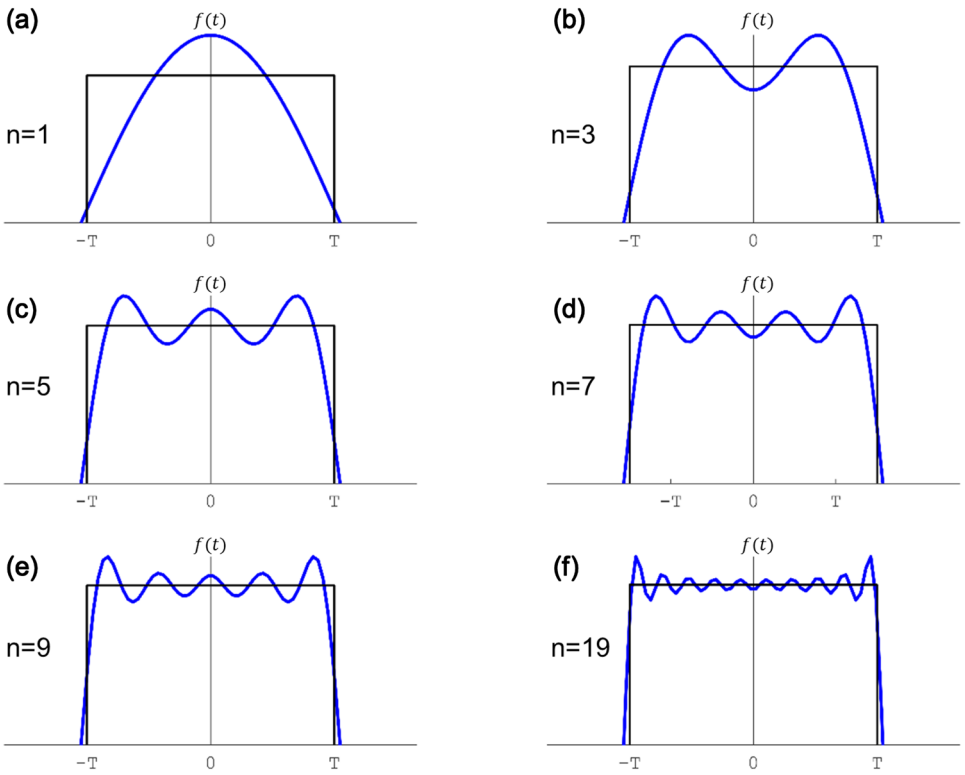

Fig. 1 Fourier series for representing a rectangle

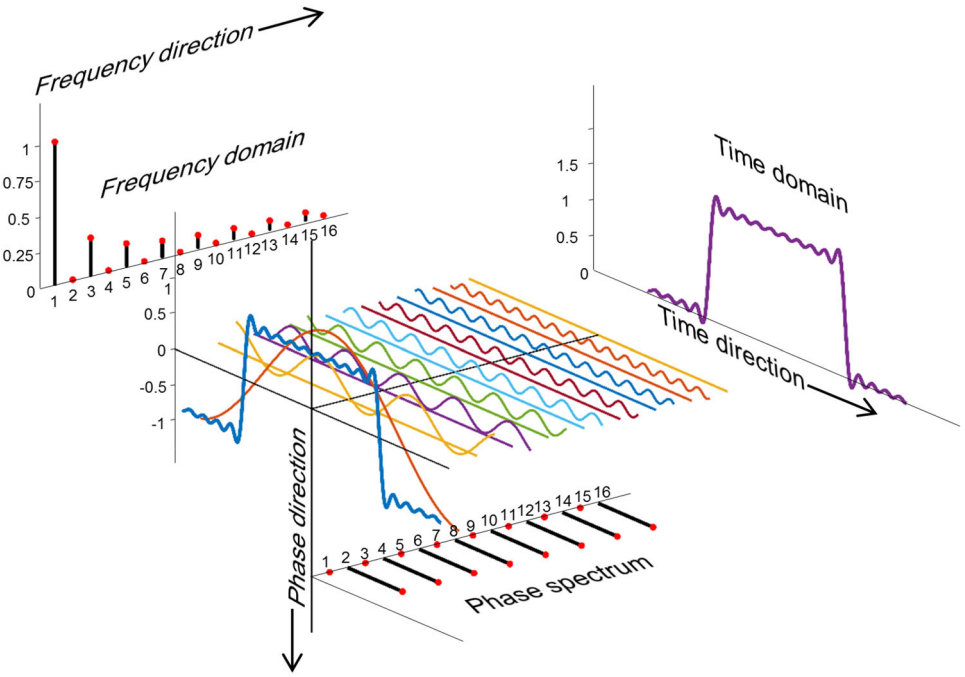

Fig. 2 Fourier expansion in time domain, frequency domain, and phase spectrum

value in phase spectrum equal to zero, while lengths of bars at odd n values in phase spectrum equal to π (we defined the range of phase spectrum in a range of $(-\pi, \pi]$).

In summary, the time domain, frequency domain, and phase spectrum solely determine a curve, which ensures the uniqueness of the Fourier series. Therefore, a 2D shape, such as the soil particle perimeter, can be expressed by either a time domain image or a frequency domain image with spectrum, as shown in Fig. 2.

3 Spherical harmonics for representing a 3D surface

Using the same concept as the Fourier series for representing 2D curves, spherical harmonics can be used to represent 3D surfaces. Fourier series uses a set of sine and cosine functions to represent 2D curves, while the spherical harmonics use a set of orthogonal spherical harmonics functions Y_n^m to represent a closed 3D geometry. A soil particle with a closed 3D surface can be represented by the spherical harmonics coefficients c_n^m and spherical harmonics functions $Y_n^m(\theta,\varphi)$:

$$r(\theta,\varphi)=\sum_{0}^{\infty}\sum_{m=-n}^{n}c_n^m Y_n^m(\theta,\varphi) \tag{4}$$

where $r(\theta,\varphi)(\theta\in[0,\pi],\ \varphi\in[0,2\pi])$ is coordinates of points on particle surface in the spherical coordinate system. The n and m are the degree and order of spherical harmonics, respectively. The base functions $Y_n^m(\theta,\varphi)$ can be determined as:

$$Y_n^m(\theta,\varphi)=\sqrt{\frac{(2n+1)(n-m)!}{4\pi(n+m)!}}P_n^m\cos(\theta)e^{im\varphi} \tag{5}$$

where P_n^m is the Legendre function. The Legendre function can be expanded by Rodrigues's formula:

$$P_n^m(x)=(1-x^2)^{|m|/2}\cdot\frac{\mathrm{d}^{|m|}}{\mathrm{d}x^{|m|}}\left[\frac{1}{2^n n!}\cdot\frac{\mathrm{d}^n}{\mathrm{d}x^n}(x^2-1)^n\right]. \tag{6}$$

Figure 3a illustrates the $Y_n^m(\theta,\varphi)$ for n = 0, 1, and 2. Figure 3b illustrates the c_n^m for n = 0, 1, and 2. The spherical harmonics coefficients c_n^m are unique for a particle. As shown in Fig. 3b, the zero degree of spherical harmonics coefficient c_0^0 determines the volume of the particle; the first degree of spherical harmonics coefficients (n = 1), including c_1^1, c_1^{-1}, and c_1^0, determines the spatial displacement of the particle relative to origin, and the second degree of spherical harmonics coefficients (n = 2), including c_2^{-2}, c_2^2, c_2^0, c_2^{-1}, and c_2^1, stores morphological properties of the particle. Despite not displaying in Fig. 3b, the larger degrees of spherical harmonics coefficients ($n>2$) also store morphological properties of the particle. Naturally, the increase in n in spherical harmonics will contain more detailed morphological properties of the particle, so the reconstructed particle will be closer to the original particle. However, high degrees will significantly increase computational loads. Researchers [36, 40, 41] have found that n = 15 provides satisfactory accuracy for particle representation and generation. Therefore, n = 15 was also used in this study.

The spherical harmonics coefficients c_n^m are a complex number:

$$c_n^m=a_n^m+b_n^m\cdot i \tag{7}$$

where a_n^m and b_n^m are the real and imaginary parts, respectively. Therefore, c_n^m can be determined as a vector in the complex plane consisting of the real axis and imagery axes. For example, nine c_n^m values for the first two degrees in Fig. 3b are plotted in the complex plane in Fig. 4a. The spatial displacement of the particle is not useful for characterizing particle shape. Therefore, the coefficients of c_1^1, c_1^{-1}, and c_1^0 are set as zeros in this study for simplicity. Due to $c_n^{-m}=(-1)^m\cdot(c_n^m)^*$ where the "*" means conjugate transposition, c_2^{-2} and c_2^2 are symmetric about the imaginary axis; c_2^{-1} and c_2^1 are symmetric about the real axis; and c_2^0 is on the real axis as shown in Fig. 4a.

The second norm of c_n^m determines the amplitude of spherical harmonics at different degree L_n:

$$L_n=\sqrt{\sum_{m=-n}^{n}\left\|c_n^m\right\|^2}\quad(n=0,\,1,\,2,\ldots,\,15). \tag{8}$$

For example, L_0 and L_2 can be expanded as:

$$L_0=\sqrt{\left\|c_0^0\right\|^2}=\left|a_0^0\right| \tag{9}$$

$$\begin{aligned}L_2&=\sqrt{\left\|c_2^{-2}\right\|^2+\left\|c_2^{-1}\right\|^2+\left\|c_2^0\right\|^2+\left\|c_2^1\right\|^2+\left\|c_2^2\right\|^2}\\&=\sqrt{(a_2^{-2})^2+(b_2^{-2})^2+(a_2^{-1})^2+(b_2^{-1})^2+(a_2^0)^2+(a_2^1)^2+(b_2^1)^2+(a_2^2)^2+(b_2^2)^2}.\end{aligned} \tag{10}$$

The L_0 represents the volume of the particle. To remove the influence of particle volume, all the L_n were divided by L_0:

$$\begin{aligned}\frac{L_n}{L_0}&=\frac{\sqrt{\sum_{m=-n}^{n}\left\|c_n^m\right\|^2}}{L_0}=\frac{\sqrt{\sum_{m=-n}^{n}\left[(a_n^m)^2+(b_n^m)^2\right]}}{L_0}\\&=\sqrt{\sum_{m=-n}^{n}\left[\left(\frac{a_n^m}{L_0}\right)^2+\left(\frac{b_n^m}{L_0}\right)^2\right]}=\sqrt{\sum_{m=-n}^{n}\left\|\widehat{c_n^m}\right\|^2}.\end{aligned} \tag{11}$$

Then, normalized spherical harmonics coefficients, $\widehat{c_n^m}$, were developed by this study by eliminating the effects of particle volume based on Eq. (11)

$$\widehat{c_n^m}=\widehat{a_n^m}+\widehat{b_n^m}\cdot i \tag{12}$$

where $\widehat{a_n^m}$ and $\widehat{b_n^m}$ are normalized real and imaginary parts as shown in Fig. 4b:

$$\widehat{a_n^m}=\frac{a_n^m}{L_0} \tag{13}$$

$$\widehat{b_n^m}=\frac{b_n^m}{L_0}. \tag{14}$$

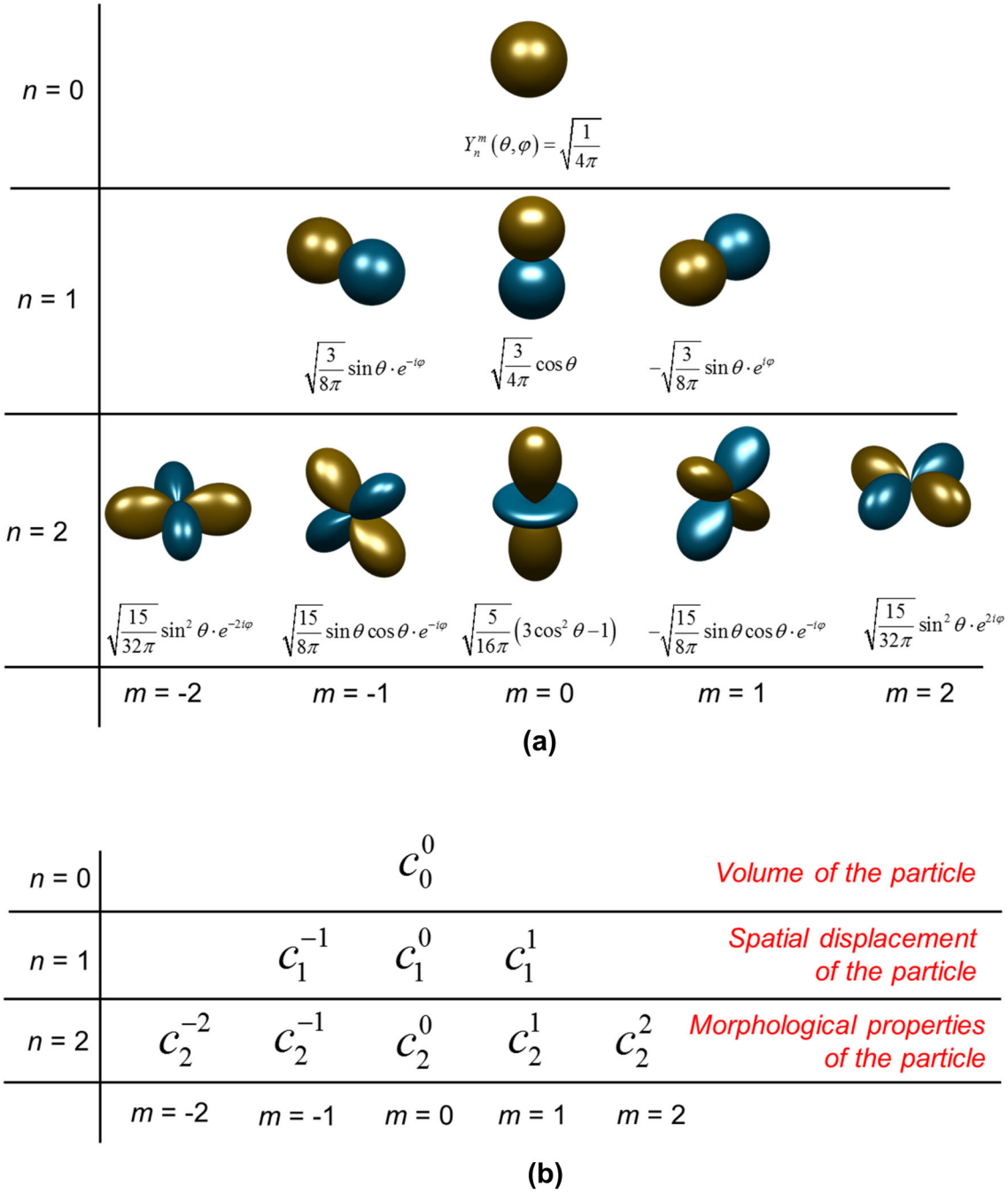

Fig. 3 Expansion of spherical harmonics for the first two degrees

A soil particle is shown in the inset of Fig. 5a. Spherical harmonics coefficients c_n^m of this particle were determined based on Eqs. (4), (5), and (6). The degree n was set as 15. Therefore, a total of 256 spherical harmonics coefficients c_n^m were computed. These c_n^m values were complex numbers based on Eq. (7). Therefore, the 256 real part a_n^m values are plotted in Fig. 5a, and the 256 imaginary part b_n^m values are plotted in Fig. 5b.

Then, the volume of the particle L_0 is computed as 8.8 based on Eq. (10), which was used to normalize spherical harmonics coefficients c_n^m to eliminate the effects of volume. The normalized real and imagery parts $\widehat{a_n^m}$ and $\widehat{b_n^m}$ were determined based on Eqs. (13) and (14) as shown in Fig. 5c, d. The $\widehat{a_n^m}$ and $\widehat{b_n^m}$ values stored the morphological properties of the particle in the inset of Fig. 5a, and they are independent of each other. Therefore, $\widehat{a_n^m}$ and $\widehat{b_n^m}$ essentially determined morphological gene of this paper.

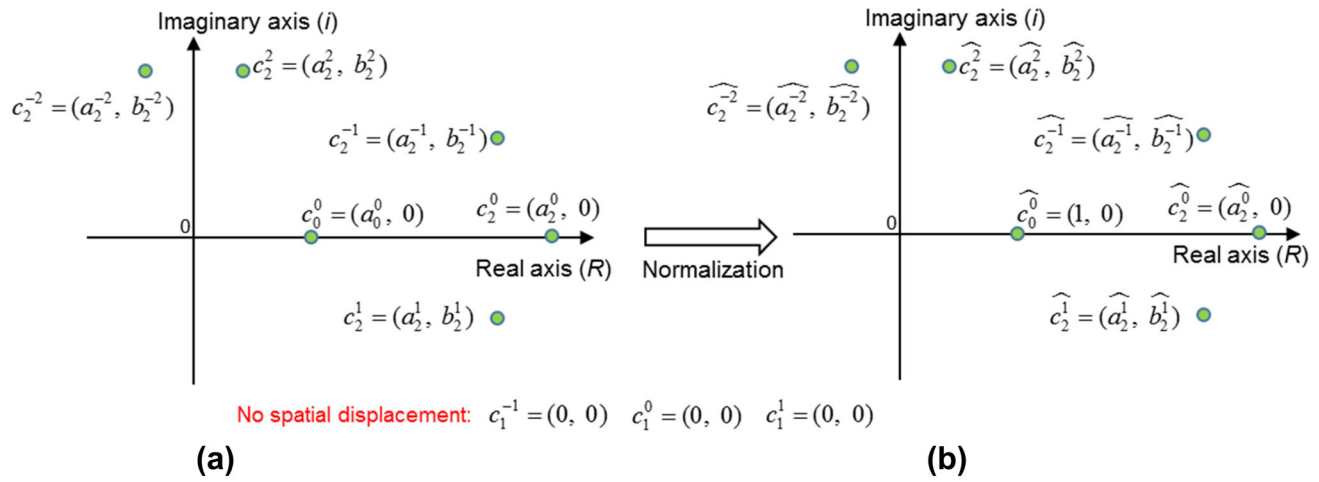

Fig. 4 The first two degrees of spherical harmonic coefficients in the complex plane

4 Integrate spherical harmonics and probability density function for particle generation

The morphology information of a particle was preserved in $\widehat{a_n^m}$ and $\widehat{b_n^m}$ values. These two values were used to fit probability functions ε_m^n. Then, the ε_m^n functions were used to generate new $\widehat{a_n^m}$ and $\widehat{b_n^m}$ values, which essentially created the morphological gene mutation. The new $\widehat{a_n^m}$ and $\widehat{b_n^m}$ values can be input into Eq. (12) to generate normalized spherical harmonics coefficients $\widehat{c_n^m}$. Then, the $\widehat{c_n^m}$ values were used in Eqs. (4), (5), and (6) to generate new particles. The new particles had similar morphological characteristics as the original particles, which will be validated by shape descriptors. It should be noted that the volume of all the generated particles is one. Users can scale up or scale down the generated particles base on the actual particle sizes.

Many probability distributions can be used in this study to generate particles, and different probability functions affect morphological gene mutations and therefore shapes of generated particles This study uses two types of probability distributions for illustration: Gaussian distribution and uniform distribution. Both distributions have simple parameters, which are easy to use and control. Specially, we found that by using the Gaussian distribution, the particle shape descriptors of generated particles were also following Gaussian distributions as will be shown shortly (Figs. 11, 12, 13, 14, 15).

To control the degree of gene mutation, a dimensionless factor η was introduced. The new $\widehat{a_n^m}$ and $\widehat{b_n^m}$ values were determined as $\eta \times \varepsilon_m^n$. Five scanned particles in Fig. 6 are used to illustrate the idea.

The uniform distributions $U(-\eta\ \widehat{a_n^m},\ \eta\ \widehat{a_n^m})$ and $U(-\eta\ \widehat{b_n^m},\ \eta\ \widehat{b_n^m})$ were used to create gene mutation. The $\widehat{a_n^m}$ was randomly selected from the range of $-\widehat{a_n^m}$ to $\widehat{a_n^m}$. The $\widehat{b_n^m}$ was randomly selected from the range of $-\widehat{b_n^m}$ to $\widehat{b_n^m}$. The η values were set as 0.1, 0.3, 0.5, 0.7, and 1.0. The generated particle shapes are shown in Fig. 6. Then, the Gaussian distributions, $N(\widehat{a_n^m},\ \eta\ \widehat{a_n^m})$ and $N(\widehat{b_n^m},\ \eta\ \widehat{b_n^m})$, were used to $\widehat{a_n^m}$ and $\widehat{b_n^m}$ values. The expectations were $\widehat{a_n^m}$ and $\widehat{b_n^m}$, respectively, and the standard deviation was the absolute values of $\left|\widehat{a_n^m}\right|$ and $\left|\widehat{b_n^m}\right|$. The η values were set as 0.1, 0.3, 0.5, 0.7, and 1.0. The generated particle shapes are shown in Fig. 6.

As the η increases, larger variations of $\widehat{a_n^m}$ and $\widehat{b_n^m}$ values were produced by probability functions, leading to a larger morphological gene mutation. Therefore, particles generated by using larger η values showed larger morphological diversities against the original particles. The next question is how to measure the morphological similarity/diversity between the original particle and generated particles. We introduced particle shape descriptors as a measure.

5 Particle shape characterizations based on computational geometry

In this study, six commonly used shape descriptors in Table 1 were used to measure morphological similarity/divergence between generated particles and the original particles. Computations of these shape descriptors needed determining principal dimensions (d_1, d_2, and d_3), volume (V), surface area (A_s), minimum circumscribed sphere, maximum inscribed sphere, and 3D convex hull. A series of computational geometry techniques were developed by

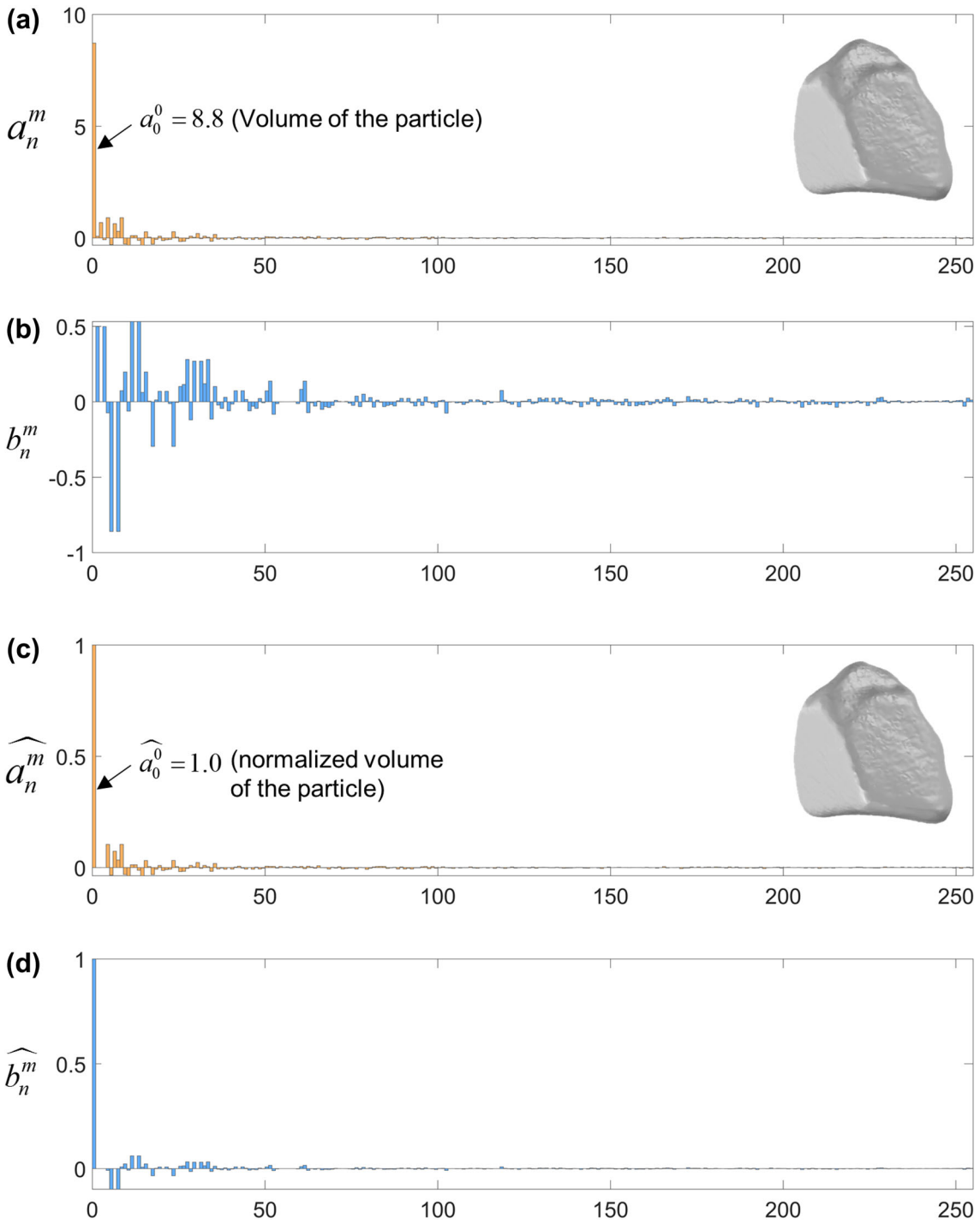

Fig. 5 The spherical harmonic coefficients and normalized spherical harmonic coefficients for a soil particle

this study to analyze 3D particle geometries to determine these parameters.

The 3D particle geometries are represented as triangular face tessellations in computer graphics as shown in Fig. 7a, b. The surface area of a given particle can be determined by the sum of the areas of all the triangular faces. A small tetrahedron is formed by connecting three vertices to the particle's centroid (O) as shown in Fig. 7b, and the volume of this tetrahedron is computed. The volume of the 3D particle (V) can then be determined by the sum of the volumes of all such tetrahedrons.

The length (d_1), width (d_2), and thickness (d_3) of a given particle geometry can be determined by a principal component analysis (PCA) [20]. For a 3D image consisting of a

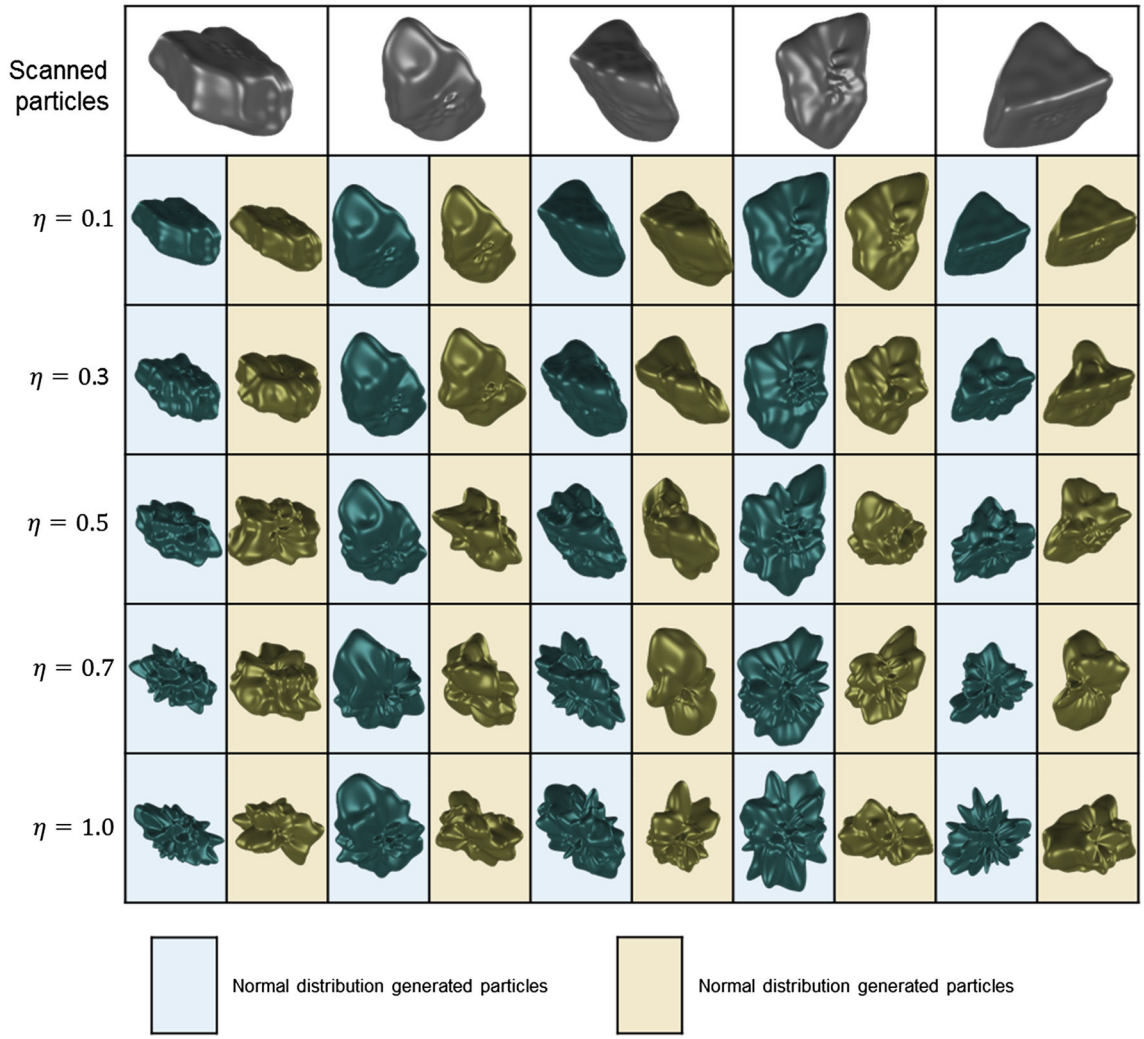

Fig. 6 Integrated spherical harmonics and probability distributions for particle generation

Table 1 Definitions of six shape descriptors

Descriptor	Formula	Note	Reference
Convexity (solidity)	$C_x = \frac{V}{V_c}$	The ratio of the volume of the particle (V) to the volume of the minimum convex hull circumscribing the particle (V_c)	Altuhafi et al. [42]
Circularity	$C = \frac{6V}{\sqrt{\frac{A_s^3}{\pi}}}$	The ratio of the volume of the particle (V) to the volume of the sphere having the same surface area (A_s) as the particle	Altuhafi et al. [42]
Intercept sphericity	$S_I = \sqrt[3]{\frac{d_2 d_3}{d_1^2}}$	The cubic root of ratio of the product of the width of the particle (d_2) and the thickness of the particle (d_3) to the square of the length of the particle (d_1)	Krumbein and Sloss [43]
Area sphericity	$S_A = \frac{V}{V_{cir}}$	The ratio of the volume of the particle (V) to the volume of the smallest circumscribed sphere (V_{cir})	Riley [44]
Diameter sphericity	$S_D = \frac{D_e}{D_{cir}}$	The ratio of the diameter of a sphere having the same volume as the particle (D_e) to the diameter of the minimum circumscribed sphere (D_{cir})	Wadell [45]
Perimeter sphericity	$S_P = \frac{A_e}{A_s}$	The ratio of the surface area of the sphere having the same volume as the particle (A_e) to the real surface area of the particle (A_s)	Altuhafi et al. [42]

point cloud, PCA can identify the largest variance of the point cloud in 3D space, which is called the first principal component. The length of the first principal component is the length (d_1) of a 3D particle. Subsequently, PCA

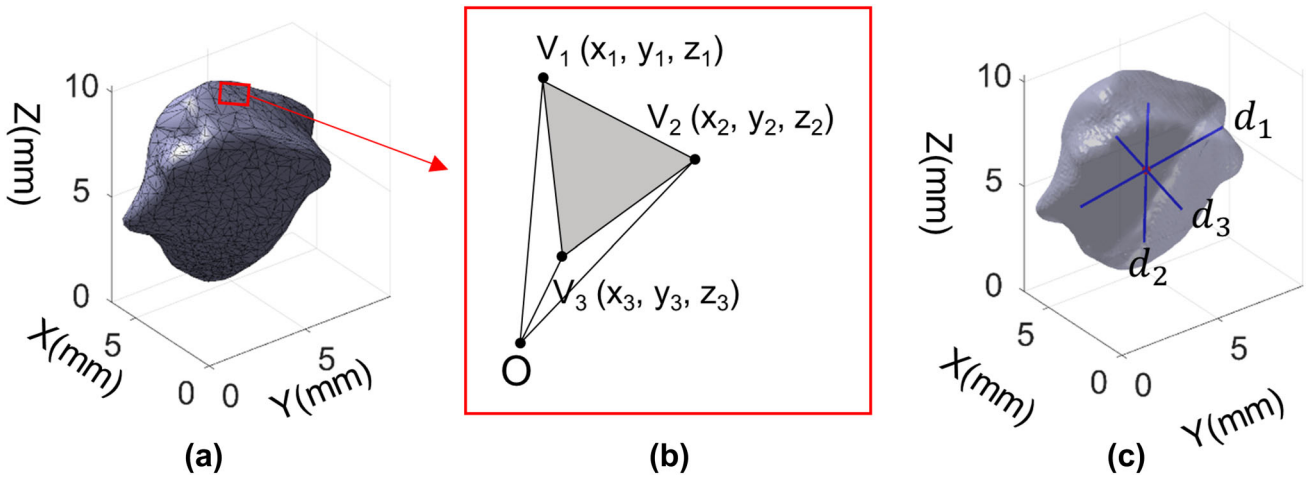

Fig. 7 Computational geometry techniques for determining surface area, volume, length, width, and thickness of a 3D particle

identifies the second largest variance, the second principal component, which is perpendicular to the first principal component, is the width (d_2) of the particle. The third principal component is perpendicular to both first and second principal components and identifies the thickness (d_3) of the particle. Figure 7c illustrates the results of a PCA analysis on a particle and shows the identified d_1, d_2, and d_3 for the particle.

The computational processes of determining the minimum circumscribed sphere and the 3D convex hull of a particle are illustrated in Fig. 8. A 2D particle is used to illustrate the concept. Points on this 2D particle boundary are shown in Fig. 8a. The minimum number of points bounding all points of the particle boundary in Fig. 8a is found as shown in Fig. 8b. This is essentially the convex hull of this particle. The same concept was used to determine the convex hull of a 3D particle as shown in Fig. 8e.

In Fig. 8b, the distance between Point 1 and Point 5 is the longest connection among points constructing the convex hull. In the first step, a trial circle is identified using

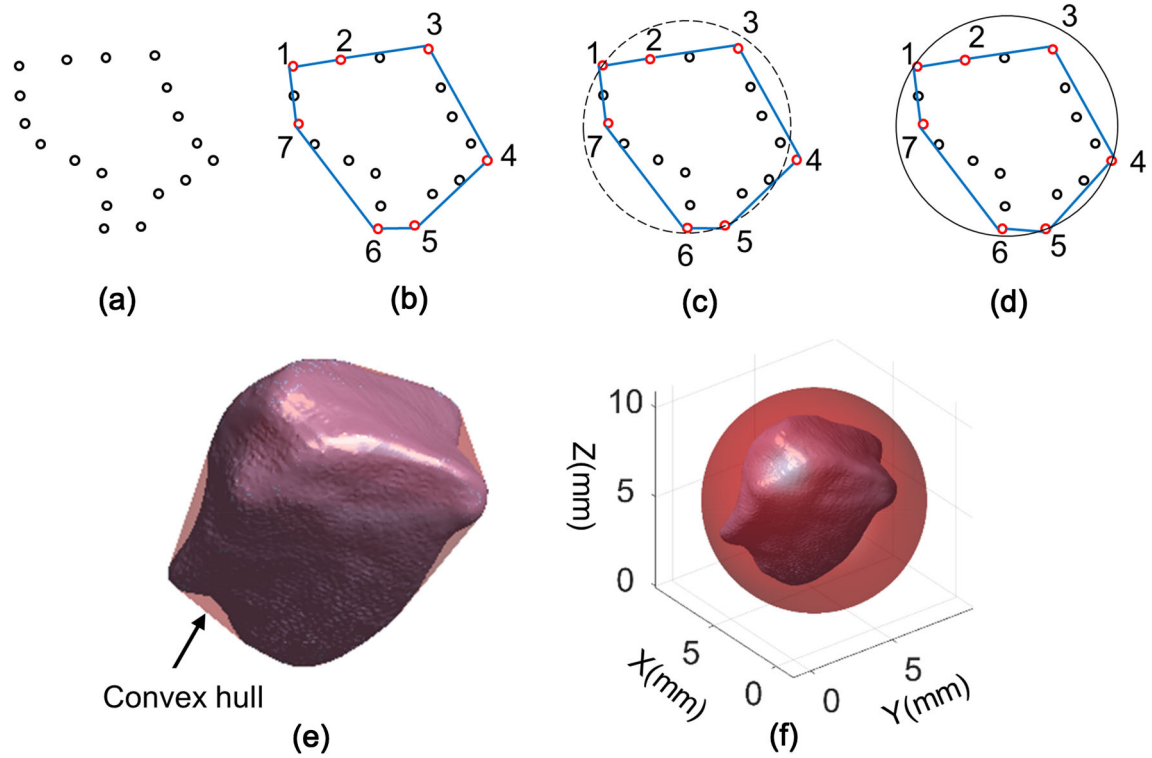

Fig. 8 Computational geometry techniques for determining convex hull and minimum circumscribed sphere of a 3D particle

Point 1 and Point 5 as the diameter in Fig. 8c. However, in this case, Point 4 is not included in the trial circle. In the second step, Points 1, 5, and 4 are used to fit a trial circle. If all the other points are within this trial circle, this is a minimum circumscribing circle. If not, the point which lies furthest outside of the trial circle is added, and a new trial circle is found using any two or three of the four points. The procedure is repeated until no point lies outside the trial circle. This yields the minimum circumscribing circle for the original set of points, as shown in Fig. 8d. The above computational process can be also applied to the 3D point cloud to identify the minimum circumscribed sphere as shown in Fig. 8f.

The maximum inscribing sphere can be determined using a 3D Euclidean transformation. For each point inside the particle in Fig. 9a, the minimum distance to the particle surface is computed, which forms a 3D Euclidean distance map, as shown in Fig. 9b. The maximum distance value in the 3D Euclidean distance map identifies the radius of the maximum inscribed sphere of the particle. The coordinates of the maximum distance value identify the center of the maximum inscribed sphere of the particle. The computed maximum inscribed sphere is superimposed within the particle in Fig. 9c.

6 Generating realistic particles based on limited morphological information

Many natural sands consist of particles having similar morphological properties because these particles have the same geological formation process. Therefore, the proposed technique can be potentially used to reproduce a soil specimen by analyzing one particle. For example, 4000 particles are randomly selected from Ottawa sand. These particles were filled into a cylinder and scanned by high-resolution X-ray computed tomography (X-ray CT) with a spatial resolution of 12 μm/voxel. The improved watershed analysis technique developed by Sun et al. [20] was used to process the X-ray CT volumetric images and identify individual particles. The result is shown in Fig. 10a. Six of the 4000 particles are zoomed in Fig. 10b.

We chose particle #5 in Fig. 10b as the base particle to generate new particles. Then, this selected particle was analyzed by spherical harmonics to determine its morphological gene (i.e., $\widehat{a_n^m}$ and $\widehat{b_n^m}$ values). Based on the morphological gene, the Gaussian distribution with $\eta = 0.5$ was used to generate new $\widehat{a_n^m}$ and $\widehat{b_n^m}$ values to create gene mutation. The new $\widehat{a_n^m}$ and $\widehat{b_n^m}$ values were used to generate 4000 particles based on Eqs. (4), (5), (6), and (14). For example, 50 generated particles are shown in Fig. 10c. The newly generated particles are visually close to the original Ottawa sand particles in Fig. 10a, b.

The computational geometry algorithm was used to determine shape descriptors for the original and generated particles as shown in Fig. 11. Particle shape distributions of original and generated particles generally agree with each other. However, as expected, they are not exactly overlapping with each other because, in natural soils, the particles shapes have some shape variations that may not be fully captured by the morphological gene of a single particle.

To evaluate the divergence of particle shape distributions of original and generated particles, a statistical approach, T test [46], is introduced. The T test computes a Z value based on standard deviations (σ) and means (μ) of two distributions:

$$Z = \frac{(\mu_1 - \mu_2)}{\sqrt{\sigma_1^2 + \sigma_2^2}} \tag{15}$$

where μ_1 and μ_2 are means of two distributions and σ_1 and σ_2 are standard deviations of two distributions. For

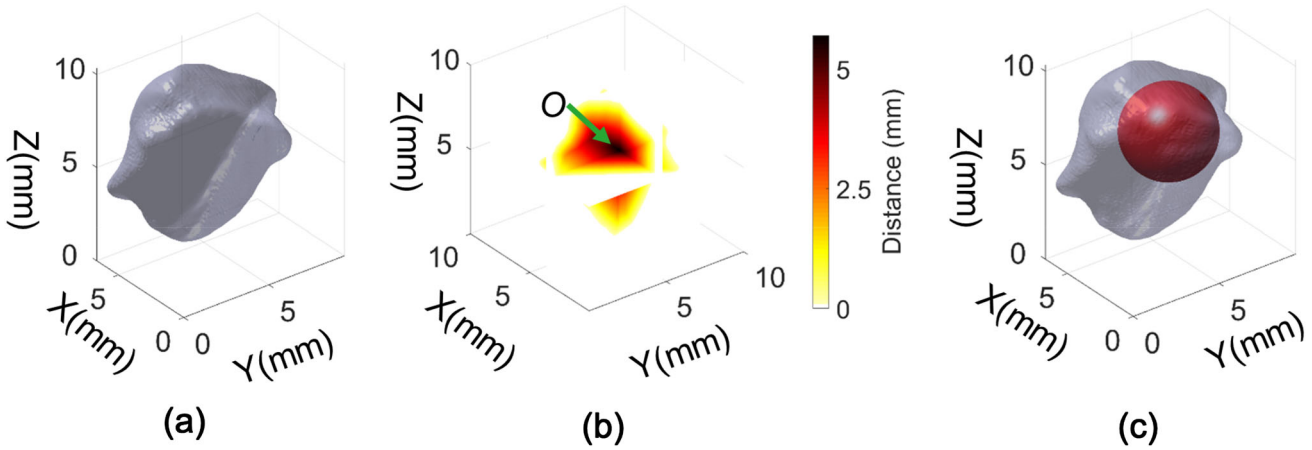

Fig. 9 Computational geometry techniques for determining the maximum inscribed sphere of a 3D particle

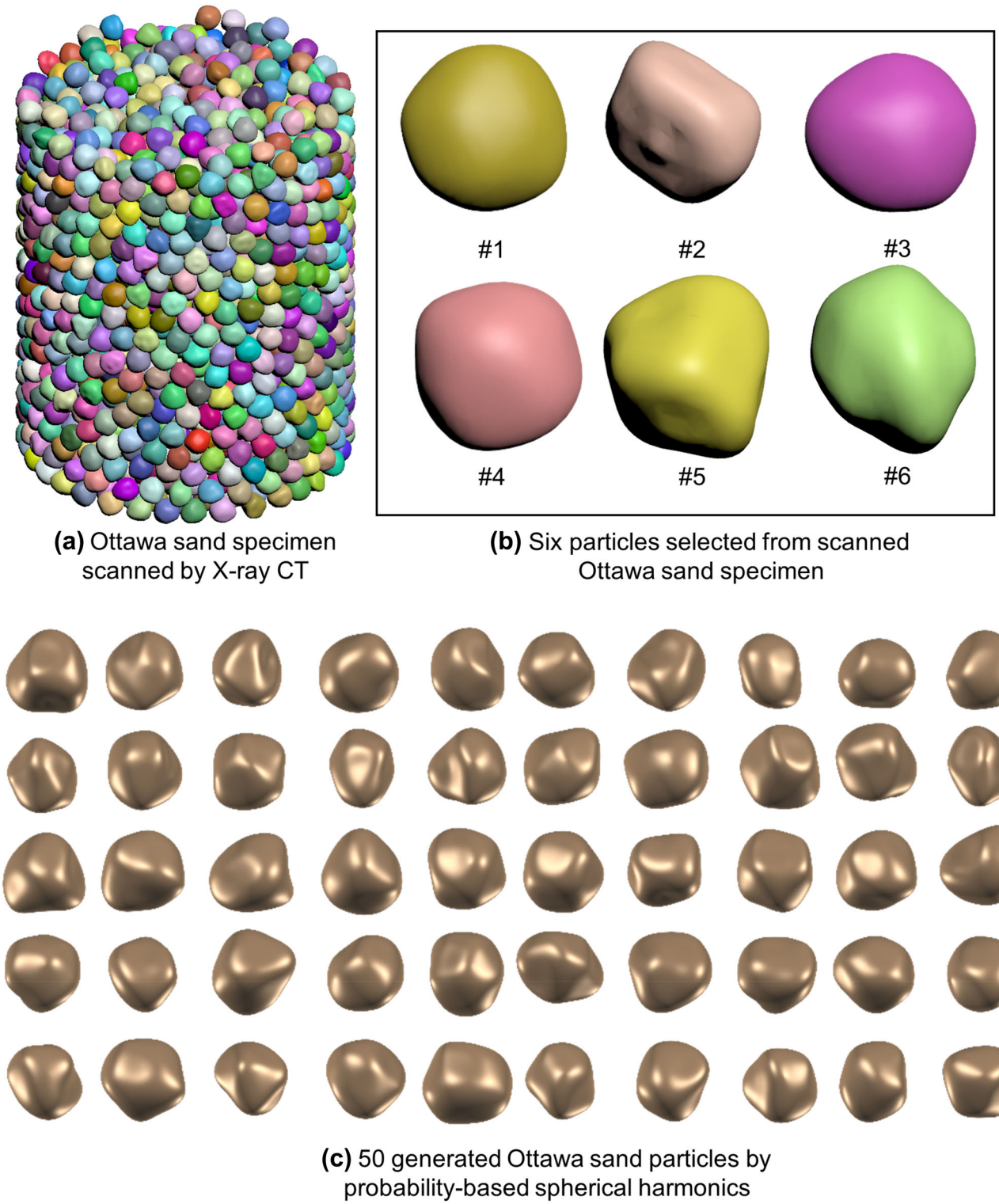

Fig. 10 Comparisons between original Ottawa sand particles scanned by X-ray CT and the generated particles by probability-based spherical harmonics

example, based on the S_A distribution of the original particles in Fig. 11d, the μ_1 and σ_1 can be computed as 0.8046 and 0.0820, respectively. Based on the S_A distribution of the generated particles in Fig. 11d, the μ_2 and σ_2 can be computed as 0.8422 and 0.0913, respectively. Therefore, the Z is computed as 0.307 as shown in Fig. 11d. The same

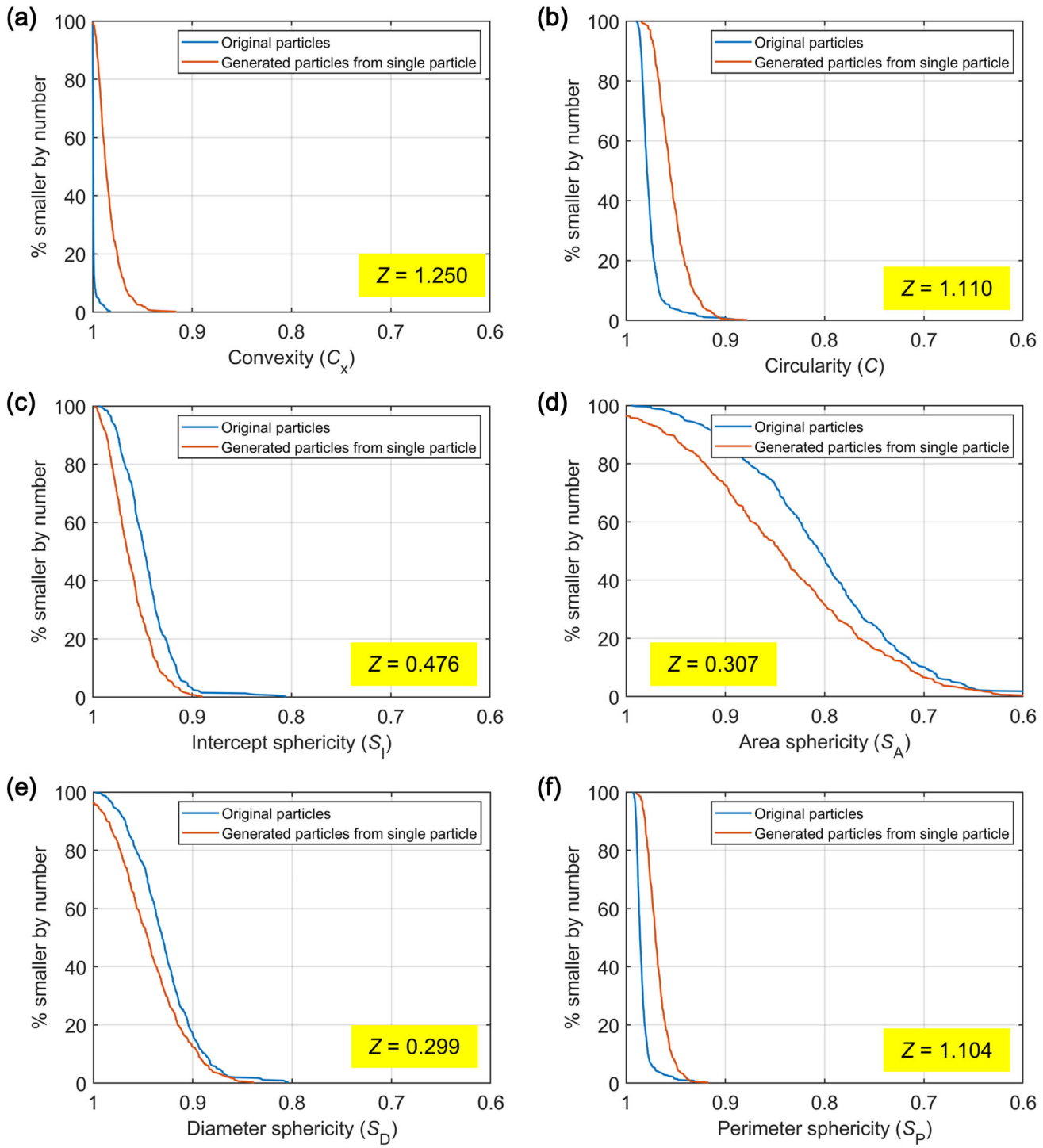

Fig. 11 Comparison between particle shape distributions of original and generated Ottawa sand particles. The original particle shape distributions are computed by analyzing 4000 Ottawa sand particles scanned by X-ray CT. Then, one Ottawa sand particle is used to generate 4000 new particles using the proposed particle clone method. The divergence of particle shape distributions of generated and original particles is evaluated by the T test

procedure is used to compute the Z values of the remaining five shape descriptors as shown in Fig. 11. If the Z value is smaller than 1.96, the two distributions are sufficiently close with a confidence level of 95% [46]. All the computed Z values are within 1.96 in Fig. 11, so the proposed particle generation technique can effectively reproduce the particle shape characteristics of original soils.

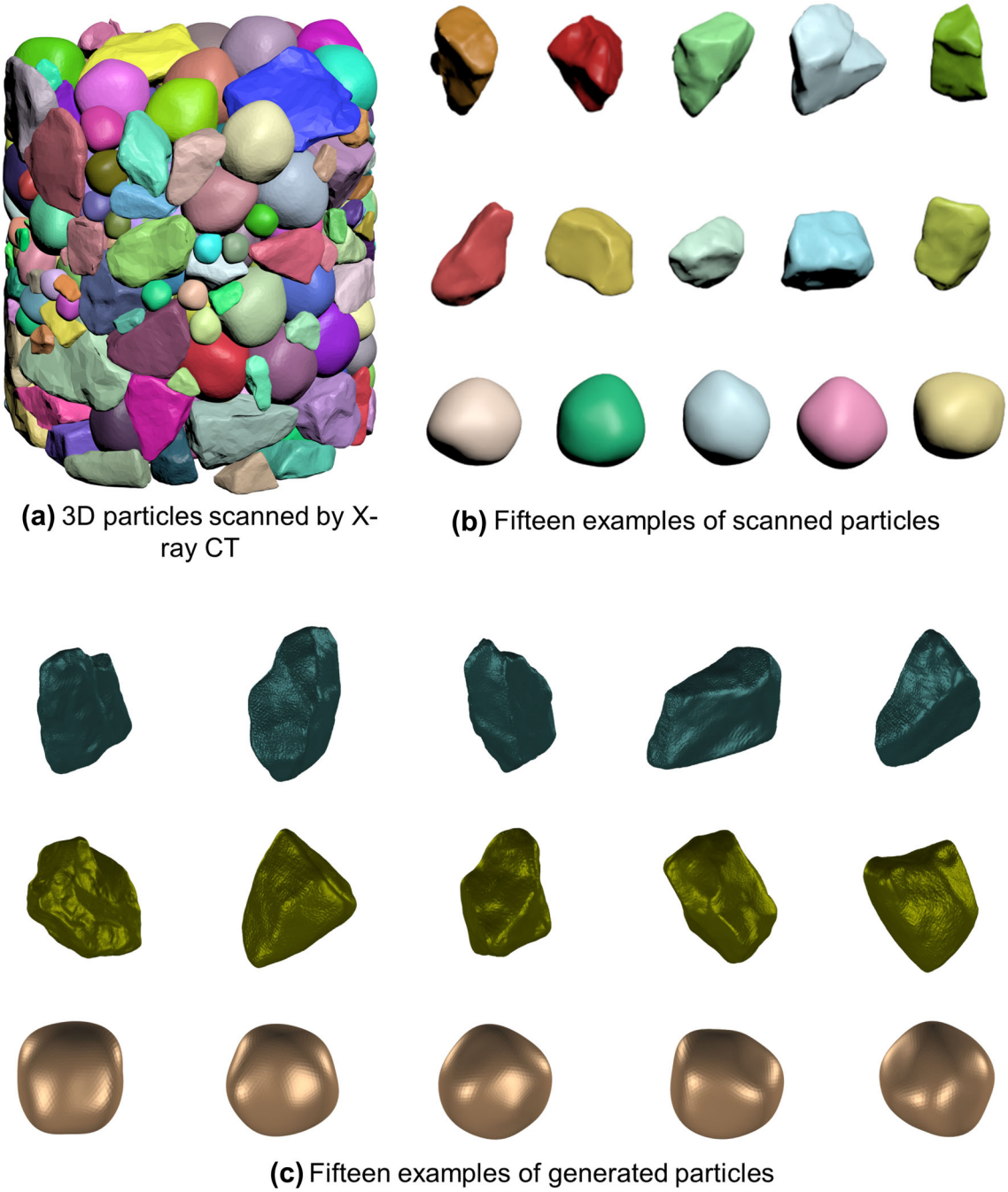

Fig. 12 Comparisons between original 214 sand particles scanned by X-ray CT and the generated particles by probability-based spherical harmonics

7 Analysis of the controlling factor η

The controlling factor η is key for governing variability and accuracy of generated particles. Large η values generate large morphological variation in the generated particles. This section investigates effects of η values on the morphological diversities in generated particles.

A total of 214 particles were selected from ten soils with disparate origins, including river alluvium, volcanic sands, colluvium, slags, crushed limestone, crushed concrete, and glass spheres. Each type contains around 21 particles in a range of 1.00 mm (#18 sieve) and 2.83 mm (#7 sieve).

To generate 3D particle geometries, a high-resolution X-ray CT is used because the X-ray CT can penetrate soil particles and capture 3D geometries of all the particles at once. Other techniques, such as the 3D laser scanner, can

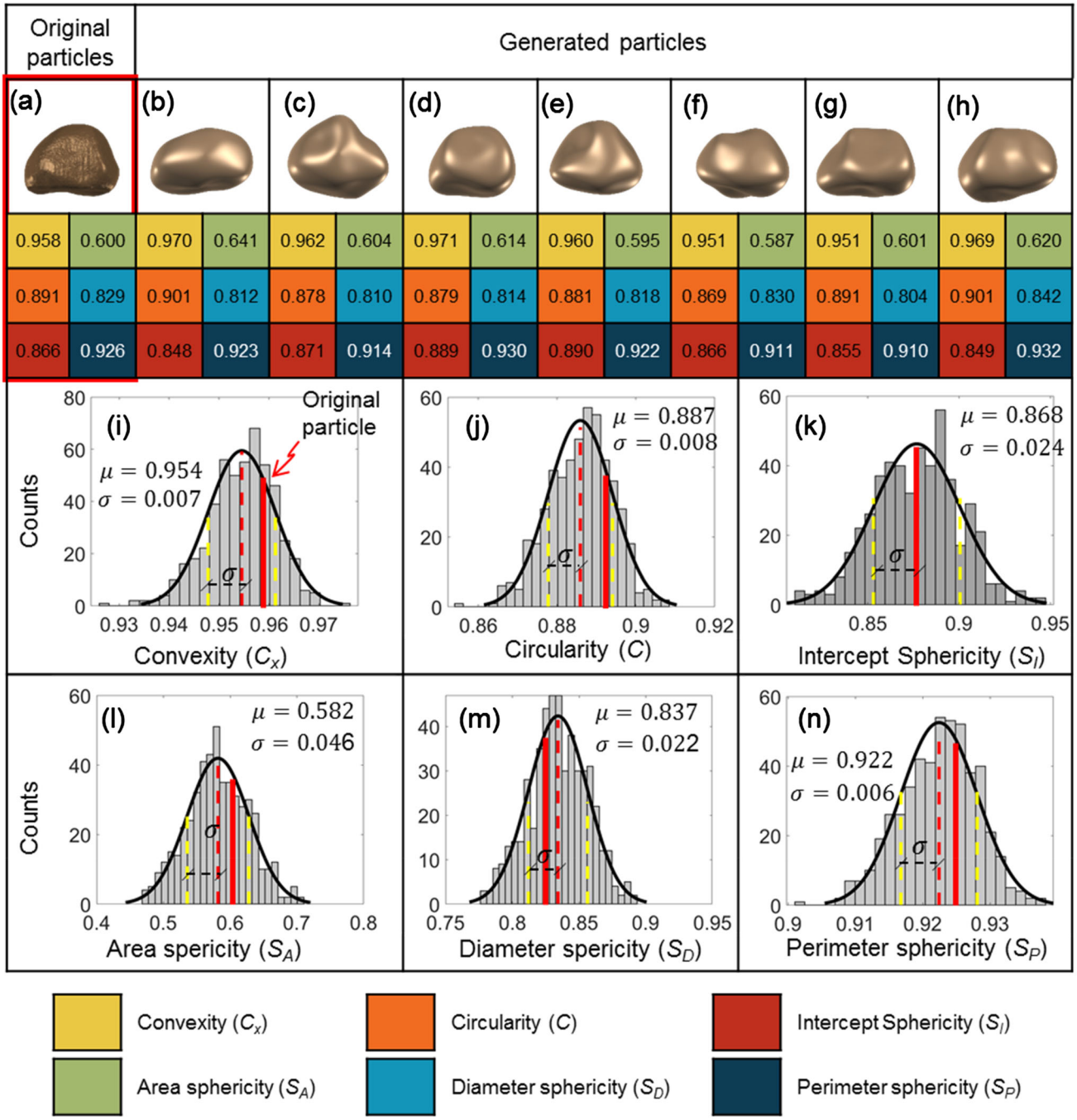

Fig. 13 Comparisons between original particles #1 and the generated particles by spherical harmonics

also be used to scan 3D particle geometries. However, the 3D laser scan must scan particles one by one and significant efforts would be required to perform 214 scans.

All the 214 particles were filled into a cylinder and scanned by high-resolution X-ray CT with a spatial resolution of 12 μm/voxel. Therefore, the 1.00 mm particle approximately has a length of 83 voxels, which is sufficient for delineating particle geometries. Therefore, we decided to scan all the 214 particles at once. The improved watershed analysis technique developed by Sun et al. [20] was used to process the X-ray CT volumetric images and identify individual particles. The result is shown in Fig. 12a.

Each of the scanned particles was analyzed to determine its morphological gene (i.e., $\widehat{a_n^m}$ and $\widehat{b_n^m}$ values). Based on the morphological gene, the Gaussian distribution with different η values was used to generate new $\widehat{a_n^m}$ and $\widehat{b_n^m}$ values and generate new particles based on Eqs. (4), (5),

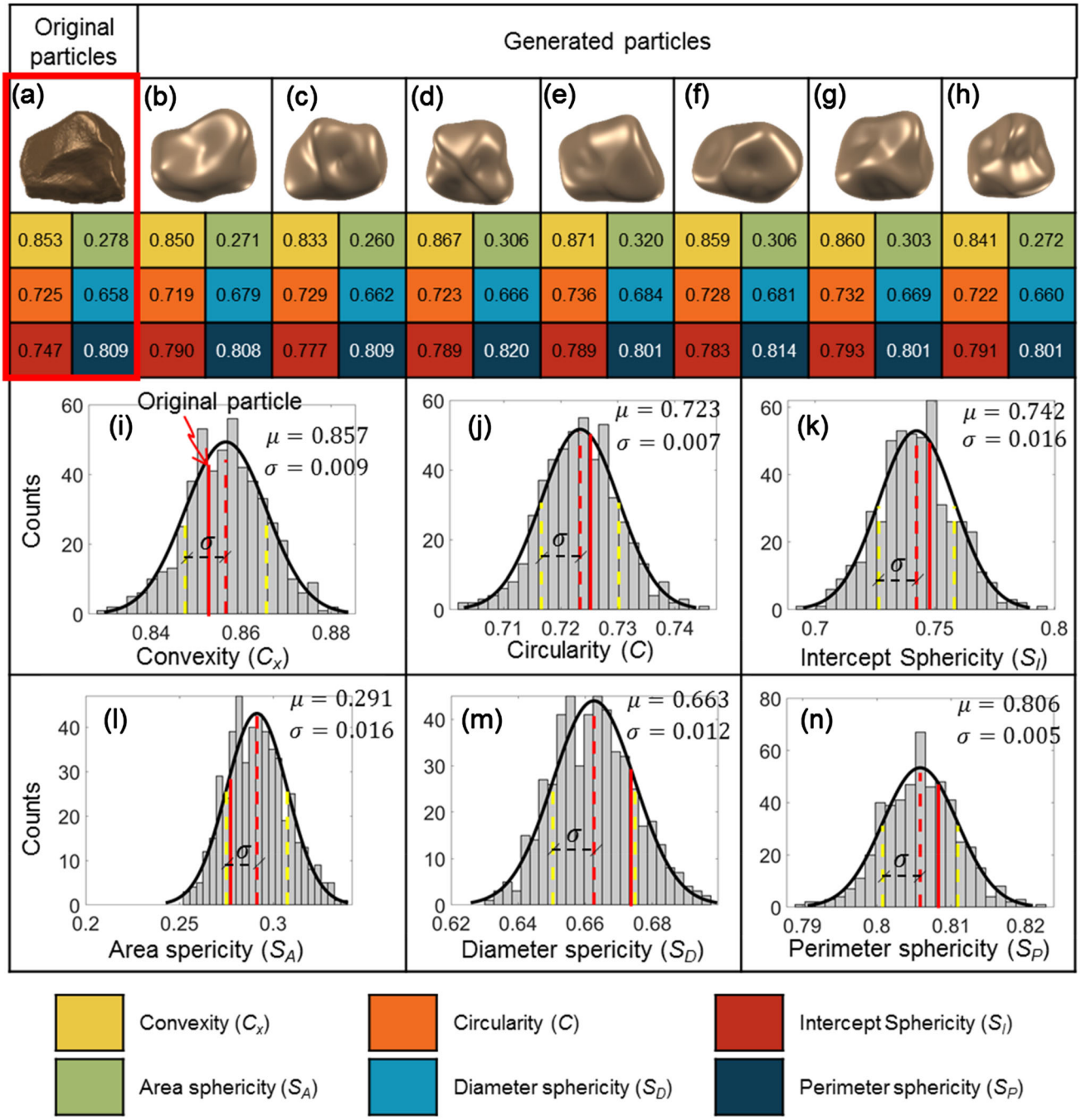

Fig. 14 Comparisons between original particles #2 and the generated particles by spherical harmonics

(6), and (14). Five η values of 0.1, 0.3, 0.5, 0.7, and 1.0 were used. A total of 500 particles are generated for each η value for each particle. Some of the original particles and generated particles are compared in Fig. 12b, c. They are visually close to each other.

The computational geometry technique is used to analyze the particle geometries and determine the particle shape descriptors of the original and generated particles. For example, Fig. 13a shows an original particle. A total of 500 particles are generated using $\eta = 0.3$, and seven of them are shown in Fig. 13b–h. The distributions of shape descriptors of the 500 generated particles are shown in Fig. 13i–n. For example, Fig. 13i shows the convexity distribution of generated 500 particles, which follows Gaussian distribution with a mean convexity μ of 0.975 and a standard deviation σ of 0.007. The convexity of the original particle is 0.978. The same comparisons were made for other three particles ($\eta = 0.3$) as shown in

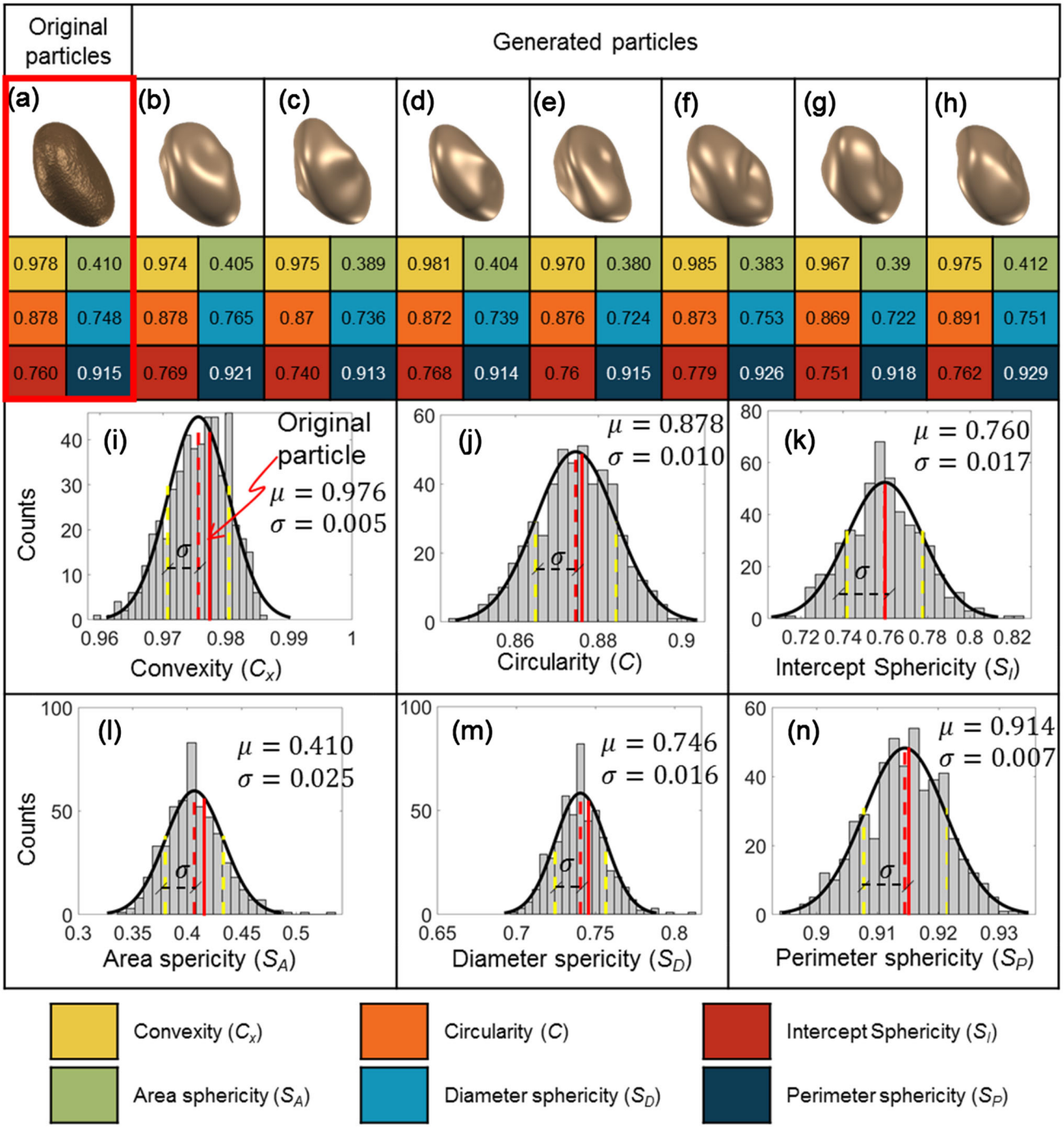

Fig. 15 Comparisons between original particles #3 and the generated particles by spherical harmonics

Figs. 14, 15 and 16. The computed particle shape descriptors of generated particles are all following Gaussian distribution. For each shape descriptor, the mean value (μ) of generated particles agrees with the value of the original particle.

Particle shape descriptors of generated particles follow Gaussian distributions, so the standard deviation σ of particle shape descriptors could be used to quantify the morphological variation in the generated particles. It is expected that large η values would provide large σ values and therefore large morphological variations in the generated particles.

As discussed before, for each η value, 500 particles are generated by cloning a particle. Therefore, for each η value, a total of 107,000 particles are generated by cloning the scanned 214 particles. For each shape descriptor, the

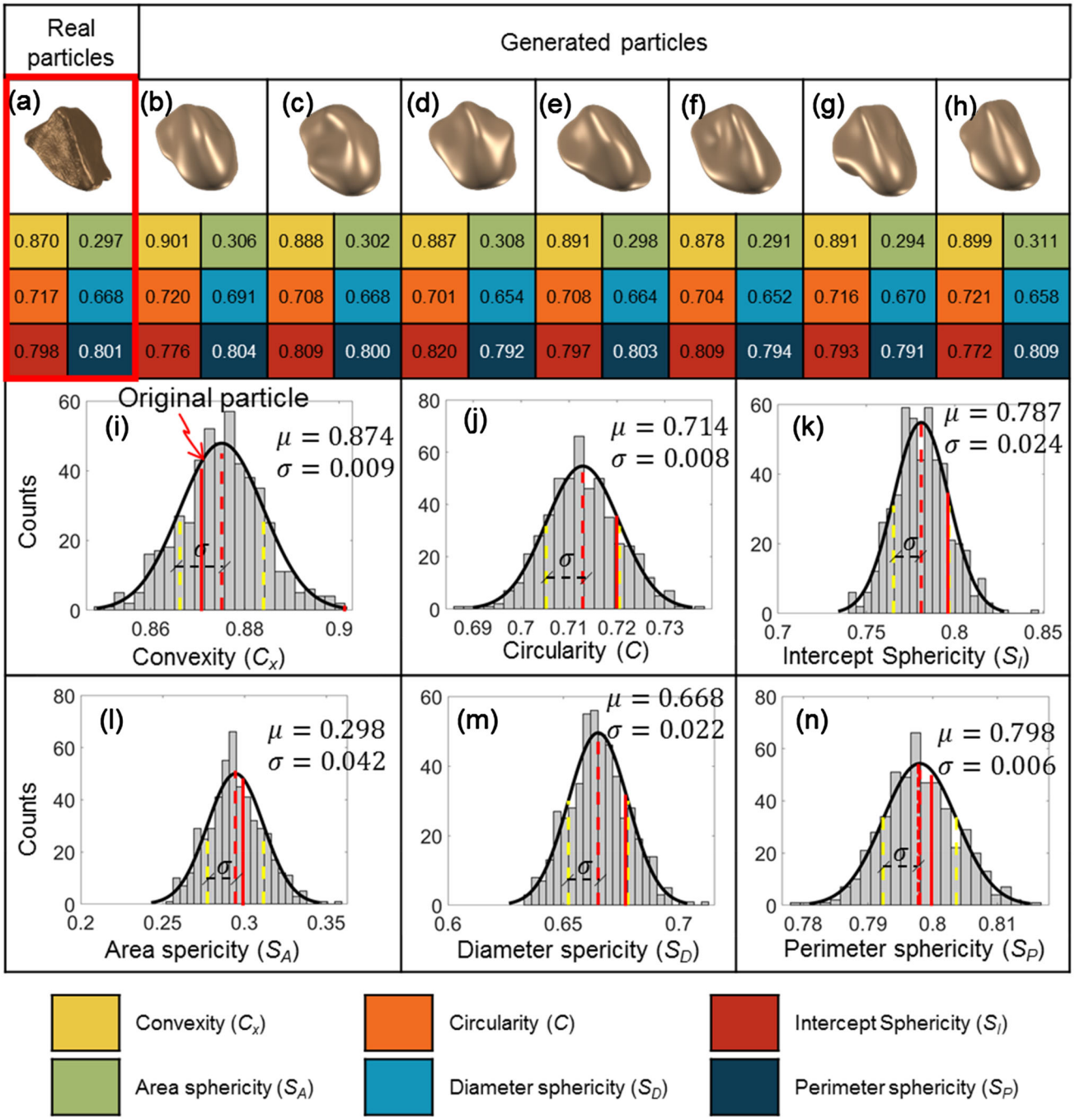

Fig. 16 Comparisons between original particles #4 and the generated particles by spherical harmonics

standard deviations of these 107,000 particles are analyzed and the average standard deviation σ is determined. The relationship between the average standard deviation σ values and different η values is shown in Fig. 17a–f. Apparently, as increasing η values, larger σ values are observed in the generated particles, resulting in larger morphological variances.

Users can use Fig. 17 to select appropriate η values based on specific problems. For example, the manufactured sands, such as Ottawa sands, crushed limestone, and slag, typically contain particles having a narrow range of particle shapes. The small η values can be used to generate particles for these sands. However, the typical natural sands contain particles having a wide range of particle shapes. The large η values can be used to generate particles for these sands.

To future validate the proposed algorithm, the particle shape distributions of generated 107,000 particles using $\eta = 0.3$ are determined as shown in Fig. 18. The particle

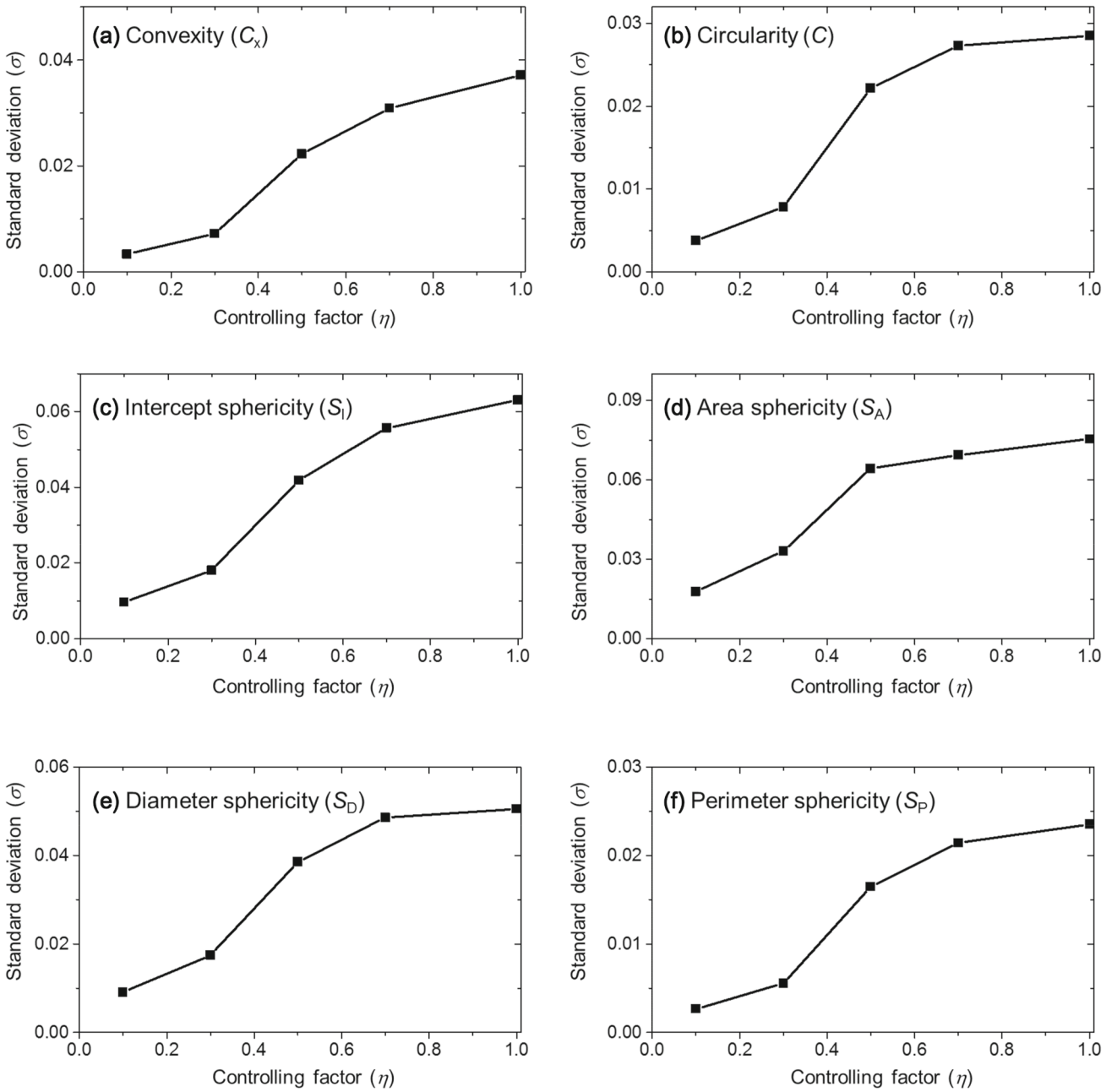

Fig. 17 Effects of η values on morphological variation ranges of generated particles

shape distributions of original 214 particles scanned by X-ray CT are also shown in Fig. 18. The T test is used to evaluate the divergence of particle shape distributions of original and generated particles following Eq. 15. The computed Z values are also shown in Fig. 18. As discussed before, if the Z value is smaller than 1.96, the two distributions are sufficiently close with a confidence level of 95%. All the computed Z values are within 1.96 in Fig. 18, so the proposed particle generation technique can effectively reproduce the particle shape characteristics of original soils.

8 Conclusions

In this paper, a probability-based spherical harmonics technique was developed. This technique can generate realistic particles based on limited morphological information. This technique analyzed a single particle and extracted spherical harmonics coefficients ($\widehat{a_n^m}$ and $\widehat{b_n^m}$ values), which are analog with the morphological gene of the particle. These $\widehat{a_n^m}$ and $\widehat{b_n^m}$ values were used to determine the probability distribution, such as Gaussian and

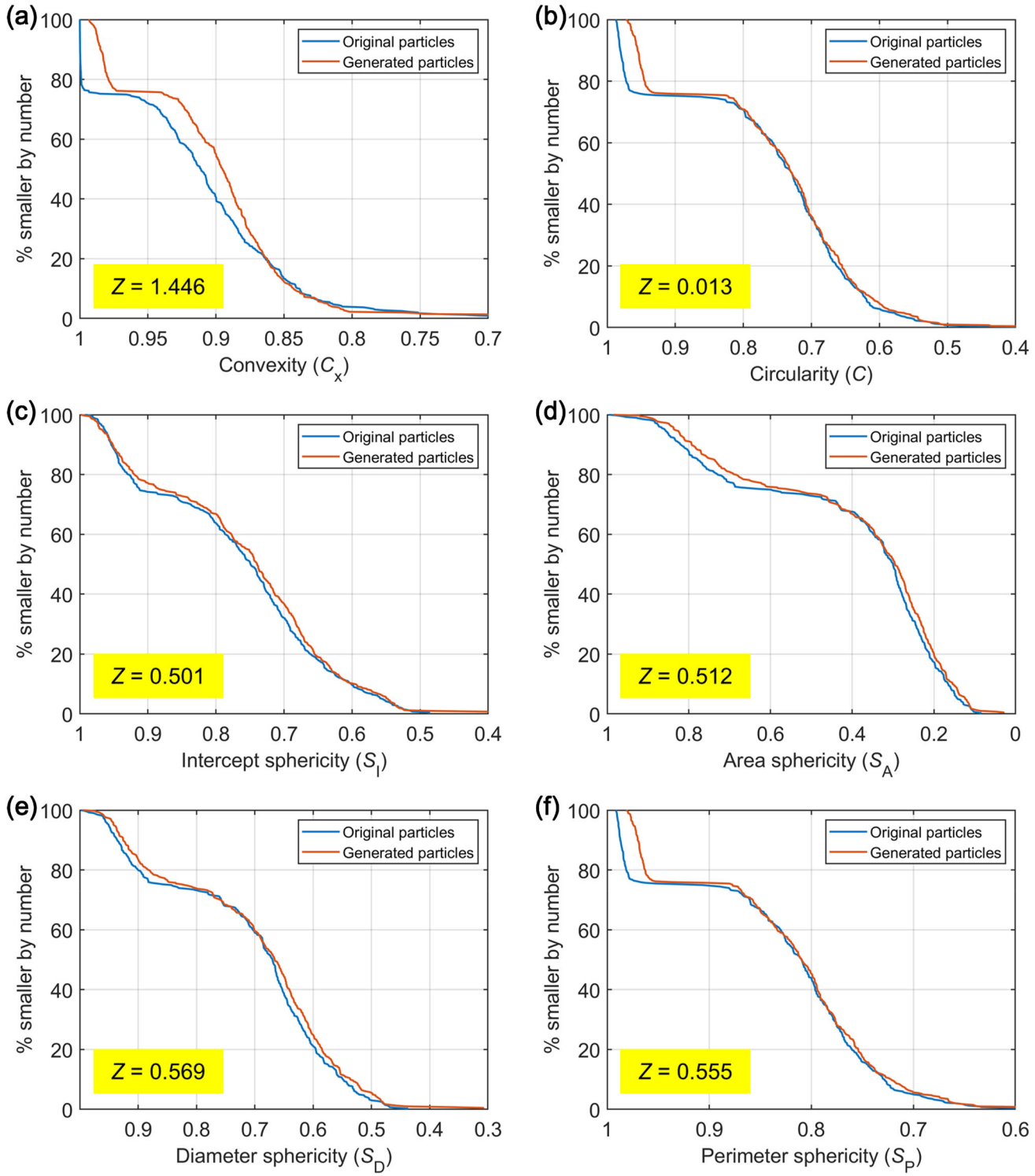

Fig. 18 Comparison between particle shape distributions of original and generated particles. The original particle shape distributions are computed by analyzing 214 particles scanned by X-ray CT. The generated 107,000 particles at $\eta = 0.3$ were analyzed to determine particle distribution of generated particles. The divergence of particle shape distributions of generated and original particles is evaluated by the T test

uniform distributions. The probability distributions were used to determine new $\widehat{a_n^m}$ and $\widehat{b_n^m}$ values, which were the analog of gene mutation. The new $\widehat{a_n^m}$ and $\widehat{b_n^m}$ values were used to generate 3D particle geometries with the same

morphological properties as the original particles. A controlling factor η was developed to tune degrees of gene mutation. Large η generated particles with a large morphological variance against the original particle.

The morphological variances between generated and original particles were quantified by six commonly used particle shape descriptors, including convexity (or solidity), circularity, aspect ratio, area sphericity, diameter sphericity, and perimeter sphericity. A series of computational geometry algorithms were developed by this research to analyze 3D particle geometries to determine these shape descriptors.

This study used X-ray CT to scan 4000 Ottawa sand particles. Then, one of the scanned particles was randomly selected to generate 4000 particles. The particle shape distributions of original and generated particle agreed well with each other. This validates the effectiveness of the proposed probability-based spherical harmonics.

A total of 214 particles with various shapes were scanned by X-ray CT. For each particle, the morphological gene is extracted. Based on the morphological gene, the Gaussian distribution with different η values was used to generate new particles. Five η values of 0.1, 0.3, 0.5, 0.7, and 1.0 were used. The original and generated particles were analyzed by computational geometry techniques to determine their shape descriptors. The dimensionless factor η controls the morphological variances of the generated particles. By using the Gaussian probability distribution, the particle shape distributions of generated particles are also following Gaussian distribution. Therefore, the standard deviation σ is used to quantify the morphological variation of generated particles. The relationship between σ and η is explored. This study may facilitate to generate realistic particle geometries for discrete element method and geo-mechanical analysis for understanding macro-engineering behavior of granular soils.

Acknowledgements This material is based upon work supported by the U.S. National Science Foundation under Grant No. CMMI 1917332. Any opinions, findings, and conclusions or recommendations expressed in this material are those of the authors and do not necessarily reflect the views of the National Science Foundation.

Compliance with ethical standards

Conflict of interest The authors declare that they have no conflict of interest.

References

1. Cho G-C, Dodds J, Santamarina JC (2006) Particle shape effects on packing density, stiffness, and strength: natural and crushed sands. J Geotech Geoenviron Eng 132:591–602. https://doi.org/10.1061/(asce)1090-0241(2006)132:5(591)
2. Altuhafi FN, Coop MR, Georgiannou VN (2016) Effect of particle shape on the mechanical properties of natural sands. J Geotech Geoenvironmental Eng 142:1–15. https://doi.org/10.1061/(ASCE)GT.1943-5606.0001569
3. Shin H, Santamarina JC (2013) Role of particle angularity on the mechanical behavior of granular mixtures. J Geotech Geoenviron Eng 139:353–355. https://doi.org/10.1061/(asce)gt.1943-5606.0000768
4. Alshibli KA, Cil MB (2018) Influence of particle morphology on the friction and dilatancy of sand. J Geotech Geoenvironmental Eng 144:04017118. https://doi.org/10.1061/(ASCE)GT.1943-5606.0001841
5. Zheng J, Hryciw RD, Ventola A (2017) Compressibility of sands of various geologic origins at pre-crushing stress levels. Geol Geotech Eng. https://doi.org/10.1007/s10706-017-0225-9
6. Jerves AX, Kawamoto RY, Andrade JE (2016) Effects of grain morphology on critical state: a computational analysis. Acta Geotech 11:493–503. https://doi.org/10.1007/s11440-015-0422-8
7. Liu X, Yang J (2018) Shear wave velocity in sand: effect of grain shape. Géotechnique 68:742–748. https://doi.org/10.1680/jgeot.17.t.011
8. Bareither CA, Edil TB, Benson CH, Mickelson DM (2008) Geological and physical factors affecting the friction angle of compacted sands. J Geotech Geoenviron Eng 134:1476–1489. https://doi.org/10.1061/(asce)1090-0241(2008)134:10(1476)
9. Zheng J, Hryciw RD (2016) Index void ratios of sands from their intrinsic properties. J Geotech Geoenvironmental Eng 142:1–10. https://doi.org/10.1061/(ASCE)GT.1943-5606.0001575
10. Zheng J, Hryciw RD (2017) Particulate material fabric characterization by rotational haar wavelet transform. Comput Geotech 88:46–60. https://doi.org/10.1016/j.compgeo.2017.02.021
11. Kandasami RK, Murthy TG (2015) Effect of particle shape on the mechanical response of a granular ensemble. In: 3rd international symposium on geomechanics from micro to macro, SEP 01-03, 2014, Univ Cambridge, Cambridge, England, pp 1093–1098
12. Nouguier-Lehon C, Cambou B, Vincens E (2003) Influence of particle shape and angularity on the behaviour of granular materials: a numerical analysis. Int J Numer Anal Methods Geomech 27:1207–1226. https://doi.org/10.1002/nag.314
13. Vangla P, Roy N, Gali ML (2017) Image based shape characterization of granular materials and its effect on kinematics of particle motion. Granul Matter. https://doi.org/10.1007/s10035-017-0776-8
14. Cavarretta I, O'Sullivan C, Coop MR (2010) The influence of particle characteristics on the behaviour of coarse grained soils. Geotechnique 60:413–423. https://doi.org/10.1680/geot.2010.60.6.413
15. Zheng J, Hryciw RD (2016) A corner preserving algorithm for realistic DEM soil particle generation. Granul Matter 18:84. https://doi.org/10.1007/s10035-016-0679-0
16. Zheng J, Hryciw RD (2017) An image based clump library for DEM simulations. Granul Matter 19:1–15. https://doi.org/10.1007/s10035-017-0713-x
17. Druckrey AM, Alshibli KA, Al-Raoush RI (2016) 3D characterization of sand particle-to-particle contact and morphology. Comput Geotech 74:26–35. https://doi.org/10.1016/j.compgeo.2015.12.014
18. Cil MB, Alshibli KA, Kenesei P (2017) 3D experimental measurement of lattice strain and fracture behavior of sand particles using synchrotron X-ray diffraction and tomography. J Geotech Geoenvironmental Eng 143:1–18. https://doi.org/10.1061/(ASCE)GT.1943-5606.0001737
19. Zhou W, Yuan W, Ma G, Chang XL (2016) Combined finite-discrete element method modeling of rockslides. Eng Comput 33(5):1530–1559

20. Sun Q, Zheng J, Li C (2019) Improved watershed analysis for segmenting contacting particles of coarse granular soils in volumetric images. Powder Technol 356:295–303. https://doi.org/10.1016/j.powtec.2019.08.028
21. Sun Q, Zheng J (2019) Two-dimensional and three-dimensional inherent fabric in cross-anisotropic granular soils. Comput Geotech 116:103197. https://doi.org/10.1016/j.compgeo.2019.103197
22. Sun Q, Zheng J, He H, Li Z (2019) Particulate material fabric characterization from volumetric images by computational geometry. Powder Technol 344:804–813. https://doi.org/10.1016/j.powtec.2018.12.070
23. Liu X, Garboczi EJ, Grigoriu M et al (2011) Spherical harmonic-based random fields based on real particle 3D data: improved numerical algorithm and quantitative comparison to real particles. Powder Technol 207:78–86. https://doi.org/10.1016/j.powtec.2010.10.012
24. Kim H, Haas CT, Rauch AF, Browne C (2002) Dimensional ratios for stone aggregates from three-dimensional laser scans. J Comput Civ Eng 16:175–183. https://doi.org/10.1061/(ASCE)0887-3801(2002)16:3(175)
25. Hayakawa Y, Oguchi T (2005) Evaluation of gravel sphericity and roundness based on surface-area measurement with a laser scanner. Comput Geosci 31:735–741. https://doi.org/10.1016/j.cageo.2005.01.004
26. Anochie-boateng JK, Komba JJ, Mvelase GM (2013) Three-dimensional laser scanning technique to quantify aggregate and ballast shape properties. Constr Build Mater 43:389–398. https://doi.org/10.1016/j.conbuildmat.2013.02.062
27. Otsubo M, O'sullivan C, Sim WW, Ibraim E (2015) Quantitative assessment of the influence of surface roughness on soil stiffness. Géotechnique 65:694–700. https://doi.org/10.1680/geot.14.T.028
28. Alshibli KA, Alsaleh MI (2004) Characterizing surface roughness and shape of sands using digital microscopy. J Comput Civ Eng 18:36–45. https://doi.org/10.1061/~ASCE!0887-3801~2004!18:1~36!
29. Zheng J, Hryciw RD (2014) Soil particle size characterization by stereophotography. In: Geotechnical special publication, pp 64–73
30. Zheng J, Hryciw RD, Ohm H-S (2014) Three-Dimensional Translucent Segregation Table (3D-TST) test for soil particle size and shape distribution. Geomech Micro Macro 1037–1042
31. Zheng J, Hryciw RD (2017) Soil particle size and shape distributions by stereophotography and image analysis. Geotech Test J 40:317–328. https://doi.org/10.1520/GTJ20160165
32. Sun Q, Zheng Y, Li B et al (2019) Three-dimensional particle size and shape characterisation using structural light. Géotechnique Lett 9:72–78
33. Jerves AX, Kawamoto RY, Andrade JE (2017) A geometry-based algorithm for cloning real grains. Granul Matter 19:1–10. https://doi.org/10.1007/s10035-017-0716-7
34. Grigoriu M, Garboczi E, Kafali C (2006) Spherical harmonic-based random fields for aggregates used in concrete. Powder Technol 166:123–138. https://doi.org/10.1016/j.powtec.2006.03.026
35. Zhou B, Wang J, Zhao B (2015) Micromorphology characterization and reconstruction of sand particles using micro X-ray tomography and spherical harmonics. Eng Geol 184:126–137. https://doi.org/10.1016/j.enggeo.2014.11.009
36. Wei D, Wang J, Nie J, Zhou B (2018) Generation of realistic sand particles with fractal nature using an improved spherical harmonic analysis. Comput Geotech 104:1–12. https://doi.org/10.1016/j.powtec.2018.02.006
37. Su D, Yan WM (2018) 3D characterization of general-shape sand particles using microfocus X-ray computed tomography and spherical harmonic functions, and particle regeneration using multivariate random vector. Powder Technol 323:8–23. https://doi.org/10.1016/j.powtec.2017.09.030
38. Baron Fourier JBJ (1822) Théorie analytique de la chaleur. F. Didot, Paris
39. Baron Fourier JBJ (1878) The analytical theory of heat. The University Press, Cambridge
40. Mollon G, Zhao J (2014) 3D generation of realistic granular samples based on random fields theory and Fourier shape descriptors. Comput Methods Appl Mech Eng 279:46–65. https://doi.org/10.1016/j.cma.2014.06.022
41. Wei D, Wang J, Zhao B (2018) A simple method for particle shape generation with spherical harmonics. Powder Technol 330:284–291
42. Altuhafi FN, O'Sullivan C, Cavarretta I (2013) Analysis of an image-based method to quantify the size and shape of sand particles. J Geotech Geoenviron Eng 139:1290–1307. https://doi.org/10.1061/(asce)gt.1943-5606.0000855
43. Krumbein WC, Sloss LL (1951) Stratigraphy and sedimentation. W.H. Freeman and Company, San Francisco
44. Riley NA (1941) Projection sphericity. SEPM J Sediment Res. https://doi.org/10.1306/d426910c-2b26-11d7-8648000102c1865d
45. Wadell H (1935) Volume, shape, and roundness of quartz particles. J Geol 43:250–280. https://doi.org/10.1086/624298
46. Sprinthall RC, Fisk ST (1990) Basic statistical analysis. Prentice Hall, Englewood Cliffs